Energy Storage Materials 57 (2023) 1–13

Contents lists available at ScienceDirect

Energy Storage Materials

journal homepage: www.elsevier.com/locate/ensm

# *In situ* formation of stable solid electrolyte interphase with high ionic conductivity for long lifespan all-solid-state lithium metal batteries

Vahid Jabbari [a], Vitaliy Yurkiv [b], Md Golam Rasul [a], Abhijit H. Phakatkar [c], Farzad Mashayek [b], Reza Shahbazian-Yassar [a,*]

[a] Department of Mechanical and Industrial Engineering, University of Illinois at Chicago, Chicago, IL 60607, USA
[b] Department of Aerospace and Mechanical Engineering, University of Arizona, Tucson, Arizona 85721, USA
[c] Department of Biomedical Engineering, University of Illinois at Chicago, Chicago, IL 60607, USA

ARTICLE INFO

*Keywords:*
Solid polymer electrolyte
Lithium polymer batteries
Lithium metal batteries
Phosphazene
Solid electrolyte interphase (SEI)

ABSTRACT

Parasitic reactions inevitably occur at the interface of lithium (Li) metal and polymer electrolytes due to ultrahigh Li reducibility coupled with poor interfacial stability or ionic conductivity. This leads to significant capacity loss and inferior lifespan of Li metal batteries (LMBs). Herein, we engineered a stable solid electrolyte interphase (SEI) layer at the interface of Li metal and polyethylene oxide (PEO) electrolyte via incorporation of phosphazene molecules. The phosphazene-solid polymer electrolyte (P-SPE) shows a significantly higher long-term stability against Li metal anode when compared with non-modified SPE. Using cryogenic transmission electron microscopy (cryo-TEM) and X-ray photon spectroscopy (XPS), $Li_3N$, LiF, $Li_3P$ and $Li_3PO_4$ nanocrystals were identified in the SEI layer. The Li|Li cell with P-SPE cycle for 1800 cycles at 0.2 mA $cm^{-2}$. The Li||LFP cells with P-SPE deliver a specific capacity of ~150 mAh $g^{-1}$ and ~120 mAh $g^{-1}$ at 1C and 2C charge/discharge rates, respectively, with up to 80% capacity retention after 500 and 1000 cycles, respectively. Critical role of phosphazene-modified SEI in improving electrochemical performance is further investigated by density function theory (DFT) and ab-initio molecular dynamic (AIMD) calculations. This study offers a promising approach for engineering a stable and ion-conductive Li|polymer electrolyte interface for long lifespan LMBs.

## 1. Introduction

Owing to lightweight (0.59 g $cm^{-3}$), high specific capacity (3860 mA h $g^{-1}$), and low reduction potential (−3.040 V vs. SHE), Li metal is an ultimate anode for future high-energy-density rechargeable batteries [1]. Inherent safety, low cost, lightweight, mechanical strength, and facile manufacturing and large-scale production make solid polymer electrolytes (SPEs) a promising electrolyte for lithium metal batteries (LMBs) [2–4]. High Li ion conductivity, and high electrochemical and thermal stability makes polyethylene oxide (PEO) one of the most promising polymer for polymer electrolytes [5,6]. Ultrahigh reactivity of Li metal leads to parasitic reactions at Li metal|PEO interface, or so-called solid electrolyte interphase (SEI), (for instance, decomposition of PEO to $C_2H_4$ or $Li_2O$), harming electrochemical performance and lifespan of LMBs [7,8]. Additionally, during the battery operation, the SEI layer can continuously build up at the Li|polymer electrolyte interface caused by repeated parasitic reactions between the Li metal and PEO, leading to uneven surface morphology and large electrochemical impedance [9,10]. During battery operation, these events occurring at the Li|PEO interface can cause in overpotential evolution, capacity loss and inferior battery lifespan [9,11].

The issue of unstable Li|PEO interface can be addressed by engineering an interphase layer with high Li ion conductivity and high stability against Li metal [12–18]. Surface coating of Li metal with fast Li ions conductors owning high mechanical and electrochemical stability, such as ($Li_3N$), lithium phosphide ($Li_3P$), and lithium phosphide ($Li_3PO_4$), is shown an effective strategy towards homogeneous Li electrodeposition and long lifespan LMBs [15,17,19–21]. However, poor interconnectivity at interface, mechanical fragility, and a relatively thick surface coating are some of the issues with *ex-situ* coating of an artificial interfacial layer. These issues can be resolved by *in situ* construction of a SEI layer with desired chemistry and structure. In fact, tuning the electrolyte composition is considered one of the most effective approaches to tailor the SEI layer properties and improving LMBs lifespan [22]. This is due to the fact that the SEI layer plays a critical role in Li plating/stripping during charge/discharge processes and hence, is a

* Corresponding author.
*E-mail address:* rsyassar@uic.edu (R. Shahbazian-Yassar).

https://doi.org/10.1016/j.ensm.2023.02.009
Received 21 October 2022; Received in revised form 17 January 2023; Accepted 4 February 2023
Available online 5 February 2023

key factor in determining platted Li morphology, power capability, cycle life, and safety of lithium batteries [17,20,23,24]. Generally, the SEI breakdown is usually observed for a SEI layer mostly consisting of amorphous organic phase or Li-based nanocrystals with poor Li ion conductivity and stability against Li metal, such as lithium oxide ($Li_2O$) and lithium carbonate ($Li_2CO_3$) [1]. In contrast, a SEI layer with high Li ion conductivity and stability against Li metal can suppress Li dendrites growth and facilitate Li ions transport across the interface, and could assure a superior electrochemical performance and lifespan for LMBs [17,19,25]. Fluorinated organic solvents and lithium nitrate ($LiNO_3$) are widely used as additives in liquid electrolytes to tune the chemistry and structure of the SEI layer. Electrochemical degradation of these additives leads to *in situ* construction of favorable nanocrystals (e.g. LiF or $Li_3N$) in the SEI layer, leading to significant improvement in the electrochemical performance and lifespan of LMBs [12,13,16,18,26]. There is also a single report on enhancing the electrochemical performance of LMBs with polymer electrolyte via SEI modification. This is achieved by *in situ* construction of LiF-rich SEI layer by adding $Li_2S$ to the PEO-LiTFSI SPE as indicated by cryo-TEM and XPS.

Herein, we report a long lifespan LMB enabled via enrichment of Li|PEO interface with $Li_3N$, LiF, $Li_3P$, and $Li_3PO_4$ nanocrystals using a small fraction of the phosphazene (ethoxy(pentafluoro)cyclotriphosphazene) additive in PEO-based SPE. The chemical structure and general properties of the phosphazene additive is shown in Table S1. Phosphazenes and polyphosphazenes have been employed as polymer electrolytes for Li metal batteries [27–29], flame retardant in solid and gel polymer electrolyte [30], polymer cross-linking agents in gel polymer electrolyte [31], and Li metal surface modification [32]. Allcock et al., reported employing polyphosphazene with a lithium sulfonimide substituent as single ion conductor [33]. A stable artificial SEI composed of phosphazene to protect Li metal anode in an Li-$O_2$ cell is also reported [32]. It is shown that high Li ion conductivity and mechanical strength of the artificial SEI could suppress the Li dendrites growth [32]. The phosphazene molecule used in our study contain nitrogen (N) and phosphorus (P) and fluorine (F) elements, and it is expected that during electrochemical cycling against Li metal, this molecule decompose and form Li-based compounds of $Li_3N$, LiF, $Li_3P$, and $Li_3PO_4$. In fact, these nanocrystals are known to possess high Li ion conductivity, high mechanical strength and superior stability against the Li metal [17,34–36]. To the best of our knowledge, this is the first report on introducing N- and P-based Li species at Li|PEO interface or the SEI layer. Using cryogenic transmission electron microscopy (cryo-TEM) coupled with energy dispersive X-ray spectroscopy (EDS) and X-ray photon spectroscopy (XPS) characterization, detailed structure and chemistry of the modified SEI layer was identified. The SEI layer derived from the phosphazene modified solid polymer electrolyte (P-SPE) is rich in $Li_3N$, LiF, $Li_3P$ and $Li_3PO_4$ nanocrystals. Long-term stability of the unmodified SPE and P-SPE against Li metal was also investigated. P-SPEs show long-term stability against Li metal (up to 1800 cycles) at 0.2 mA $cm^{-2}$. Li||LFP cells made using the P-SPE display an initial capacity value of ~150 mAh $g^{-1}$ and ~120 mAh $g^{-1}$ at 1C and 2C charge/discharge rate, respectively, with up to 80% capacity retention after 500 and 1000 cycles, respectively, and >99% Coulombic efficiency. This superior electrochemical performance is attributed to the presence of N, F, and P-rich interface. Ab-initio molecular dynamics (AIMD) simulation indicate degradation of the phosphazene molecule into N, F, and P elements, which can form the $Li_3N$, LiF, $Li_3P$ and $Li_3PO_4$ species in the presence of Li ions. The critical role of $Li_3N$, LiF, $Li_3P$ and $Li_3PO_4$ in improving the electrochemical performance is supported by density functional theory (DFT) calculations.

## 2. Results and discussion

### 2.1. Synthesis and characterization of the control and modified SPEs

The schematic illustration of the preparation of the C-SPE and P-SPE is shown in Fig. 1a-c. A photograph of the P-SPE punched into circular disk is also shown in Fig. 1d. Initially, the thermal and electrochemical properties of the C-SPE and P-SPE are investigated. The melting temperature ($T_m$) and crystallization temperature ($T_c$) obtained by DSC are shown in Fig. 1e. The P-SPE shows $T_m$~ 50 °C during heating cycle and $T_c$~ 16 °C during cooling cycle. These values are very similar to the C-SPE ($T_m$~ 52 °C, $T_c$~ 19 °C). Thus, it can be suggested that the low dosage of phosphazene additive within the SPE does not significantly influence mobility of the PEO polymer chains [37]. TGA also shows a similar thermal degradation pattern for both control and modified SPEs, further indicating no considerable change in the composition of SPEs by the addition of the phosphazene (Fig. 1f). Electrochemical stability of the SPEs is measured by CV from open-circuit voltage to 5 V as shown in Fig. 1g,h. The C-SPE is stable up to ~4.5 V, and the peak at ~4.5 V can be attributed to the irreversible oxidative degradation of PEO [27,38]. The CV curves of the P-SPE also show a small and a large electrochemical degradation signal at ~3.4 V and ~3.8 V, respectively. These peaks can be attributed to the electrochemical degradation of phosphazene additive inside the P-SPE which match the signals observed by the LSV scan of pure phosphazene (Fig. S1). The electrochemical degradation of the phosphazene could lead to *in situ* formation of desired nanocrystals ($Li_3N$, LiF, $Li_3P$ and $Li_3PO_4$) within the modified SEI layer. A similar electrochemical degradation of phosphazenes is reported elsewhere [39–44]. Furthermore, these peaks gradually disappear with further cycling, indicating constant degradation of the phosphazene additive inside the P-SPE (Fig. 1h). This denotes that the overall electrochemical stability window of the P-SPE is similar to that of the C-SPE within several electrochemical cycles (after full decomposition of the phosphazene). This is because there is only 2 wt% of the phosphazene in the P-SPE and the electrochemical stability window of the P-SPE is mainly determined by PEO and LiTFSI rather than the phosphazene additive. Bulk Li ion conductivity of the SPEs is also measured at different temperatures, and the corresponding results are shown in Fig. 1h. According to the findings, the both the C-SPE and P-SPE show a similar ionic conductivity.

### 2.2. Long-term stability of the control and modified SPEs against Li metal

Li plating/stripping in symmetric Li|Li cells are explored using the C-SPE and P-SPE to evaluate the long-term stability of the engineered SPE against Li metal anode. Galvanostatic Li plating/stripping in symmetric Li|Li cells with the C-SPE and P-SPE are shown in Fig. 2a-c. Measurements are performed at 0.2 mA $cm^{-2}$ current density with 30 min of Li plating/stripping. As it can be seen, the voltage polarization is lower in the case of the P-SPE. The Nyquist plots for the fresh state (before cycling) of the Li|Li cell with the P-SPE, after the first charge, and after the final discharge are also illustrated in Fig. S2. As can be see, the cell impedance somewhat increases upon cycling, indicating no short-circuit of the Li|Li cell during cycling. Moreover, the interface between the Li metal anode and C-SPE seems unstable, leading to significant fluctuations in overpotential followed by a sudden drop and finally the cell short-circuit. These fluctuations can be attributed to the poor stability and Li ions conductivity of traditional SEI components (e.g. $Li_2O$, $Li_2CO_3$) against Li metal [45]. It is also well-known that poor Li ion conductivity of the SEI layer leads to the formation of Li dendrites which can grow and cause in a short-circuit by penetrating through the SPE [46]. On the other hand, a long-term stability could be observed for the symmetric Li|Li cell with the phosphazene-modified SPE, indicating stable nature of the interface potentially due to the formation of SEI components with high stability and Li ion conductivity. In fact, previous reports demonstrate very stable nature of $Li_3N$, $Li_3P$, and $Li_3PO_4$ against Li metal and their high Li ion conductivity [15,19,20,47].

To explore the Li platting behavior in the C-SPE and P-SPE, topology and morphology of the deposited Li particles is investigated using symmetric Li|Li coin cells (Figs. 2d,e and S3). It is known that electrodeposition behavior of Li is affected by the electrolyte chemistry [48]

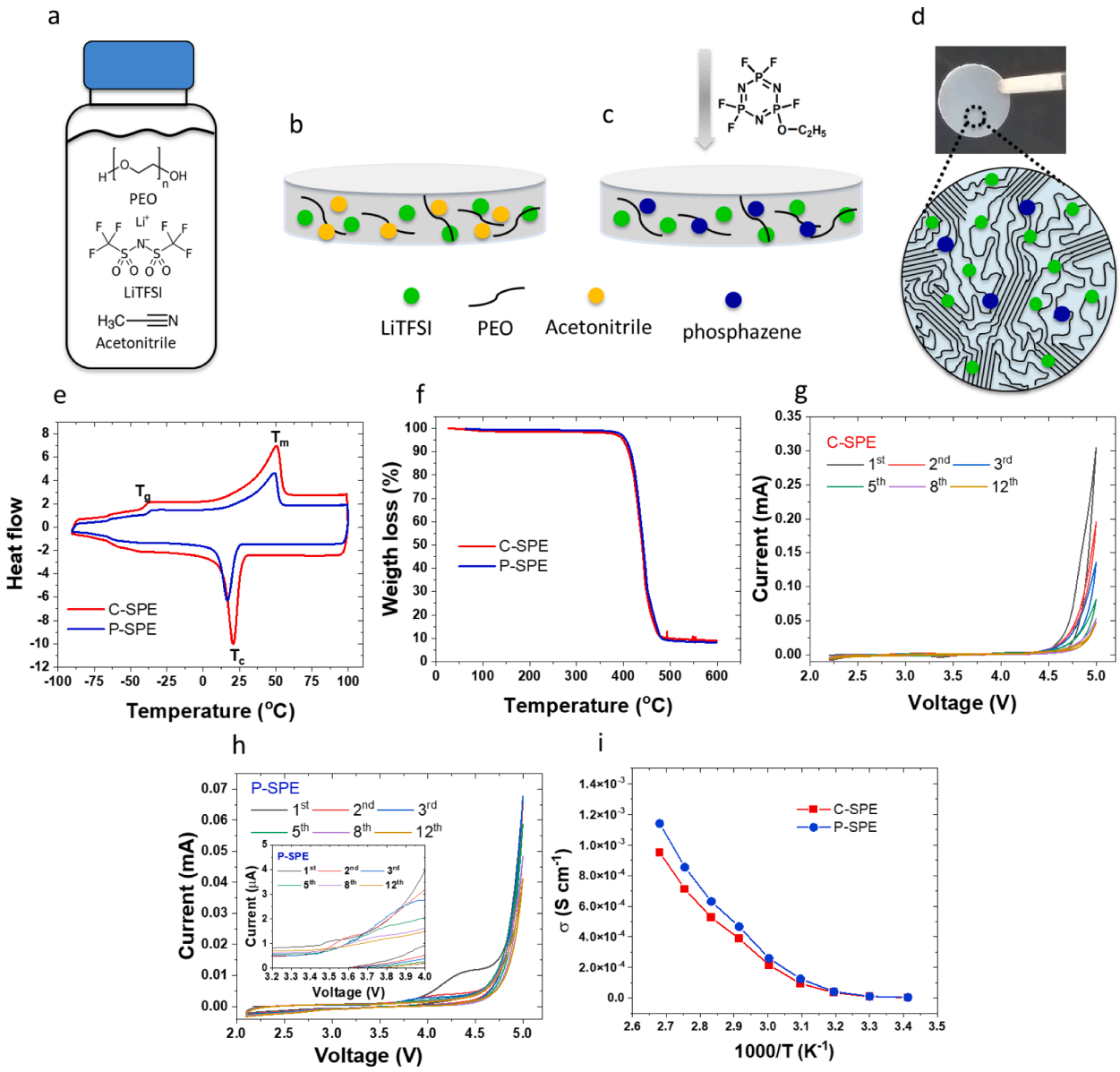


**Fig. 1.** Synthetic procedure for the SPEs preparation. (a,b) Schematic illustration of preparation and casting of the SPE precursor. (c) Dispersing the phosphazene additive into the SPE after removing the solvent under vacuum. (d) Semicrystalline P-SPE made of the phosphazene modified PEO-LiTFSI SPE, and schematic illustration of its molecular structure. (e) DSC curve of the C-SPE and the P-SPE. The data shown are for the second heating cycle at heating rate of 10 °C/min. (f) TGA curves of the C-SPE and the P-SPE. CV scans of the C-SPE (g) and the P-SPE (h) from open-circuit voltage to 5 V. Inset at (h) shows magnified CV curves of the P-SPE between 3.2 V and 4 V. (i) Temperature-dependent Li-ion conductivity of the C-SPE and the P-SPE.

and the SEI structure and composition [48]. An uneven and heterogenous Li electrodeposition is observed in the case of the control SPE (Fig. 2d). Such morphology of Li electrodeposition is reported in several studies for PEO-based polymer electrolytes [49], which can be possibly correlated to the SEI layer at the Li|PEO interface which owns poor ionic conductivity, mechanical robustness and stability against the reactive Li metal. It is also important to note that this morphology can result in significant consumption of the electrolyte constituents, leading to the formation of thick SEI layer that raise the battery cell impedance and likelihood of internal short-circuit. These unfavorable incidents results in capacity loss and low Coulombic efficiency, and decreasing lifespan of LMBs [50]. In contrast to the control SPE, a uniform and even Li platting is observed in the case of the P-SPE (Fig. 2e) which can be ascribed to regulation of Li ions flux at the interface of Li metal anode and the polymer electrolyte.

### 2.3. Chemical and structural analysis of the SEI layer at nanoscale

To further understand the interface of Li metal with the SPEs, we investigated the SEI layer formed in the control and modified SPEs at nanoscale by cryo-TEM. In order to prepare the Li deposits for TEM investigation, Li is electrochemically deposited onto a bare Cu foil within a Li|Cu cell with the C-SPE and P-SPE, at current density of 0.5 mA $cm^{-2}$. Fig. S4 shows voltage profiles of Li metal electrodeposition onto Cu foils for the control and modified SPEs. A voltage drop at the initial stage of the Li deposition followed by a flat plateau is observed, corresponding to the nucleation region (the nucleation overpotential) and the growth region (the plateau overpotential), respectively [51]. Magnitude of the nucleation overpotential defines the nucleation barrier between the Li and Cu for the electrodeposition. To evaluate Li ion transfer capability of the P-SPE, cycle performance of the Li|Cu cell with the P-SPE is also shown in Fig. S5. As can be seen, the P-SPE shows high

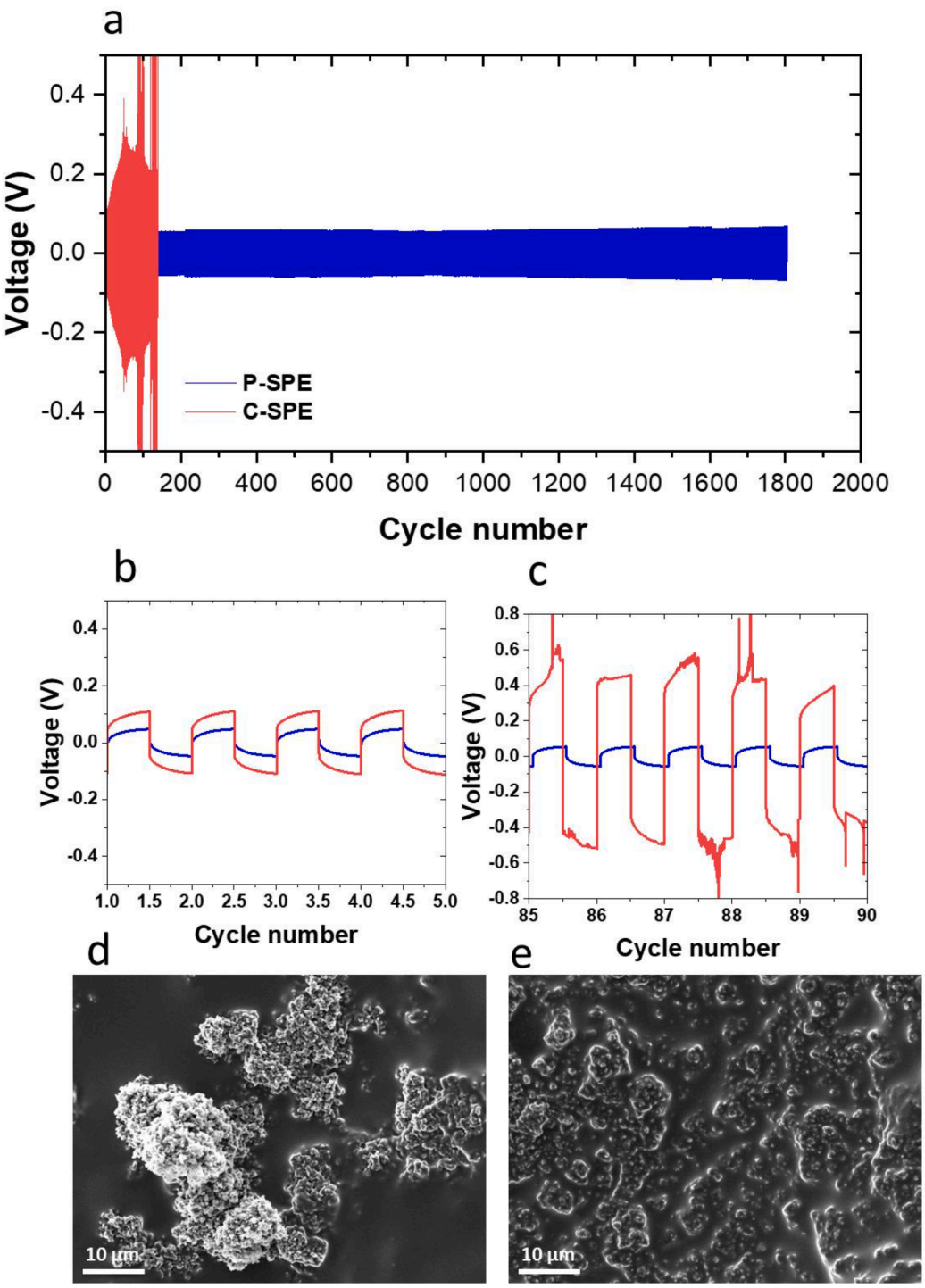


**Fig. 2.** (a) Overpotential profile of Li|Li cells with the C-SPE and the P-SPE. Magnification of voltage profiles for 1st–5th cycles (b) and 85th-90th cycles (c). Cycling is performed at constant current density of 0.2 mA $cm^{-2}$ for plating/stripping time of 30 min, at 80 °C. SEM images of the surface of Li metal anode after five Li plating/stripping cycles in the C-SPE (d) and P-SPE (e). Li platting is performed at a constant current density of 0.2 mA $cm^{-2}$ for 30 min of plating/stripping time, at 80 °C.

Li ions transferability as indicated by the high Li stripping/platting efficiency and low cell polarization. Cryo-TEM was performed to identify the chemistry and structure of the SEI layer formed in the C-SPE and P-SPE. Figs. 3a and 4a exhibit the cryo-TEM images of the Li metal deposits onto the Cu grid in the C-SPE and P-SPE, respectively, after the first Li discharge (platting). The SEI layer formed in the C-SPE shows a mosaic-type nanostructure, whereas Li-based inorganic nanocrystals are embedded within an amorphous organic/polymeric phase (Fig. 3b) [48, 52,53]. It is well-known that inorganic and organic decomposition products derived from the electrolyte can be heterogeneously distributed throughout the SEI, forming a mosaic-type microphases containing both crystalline and amorphous phases [54]. The presence of crystalline nanograins is also confirmed by selected fast Fourier transform (FFT) pattern illustrated in Fig. 3c. High resolution TEM (HRTEM) images were also captured to study nanostructure and chemistry of the Li|C-SPE interface. HRTEM images of the crystalline inorganic grains of the SEI

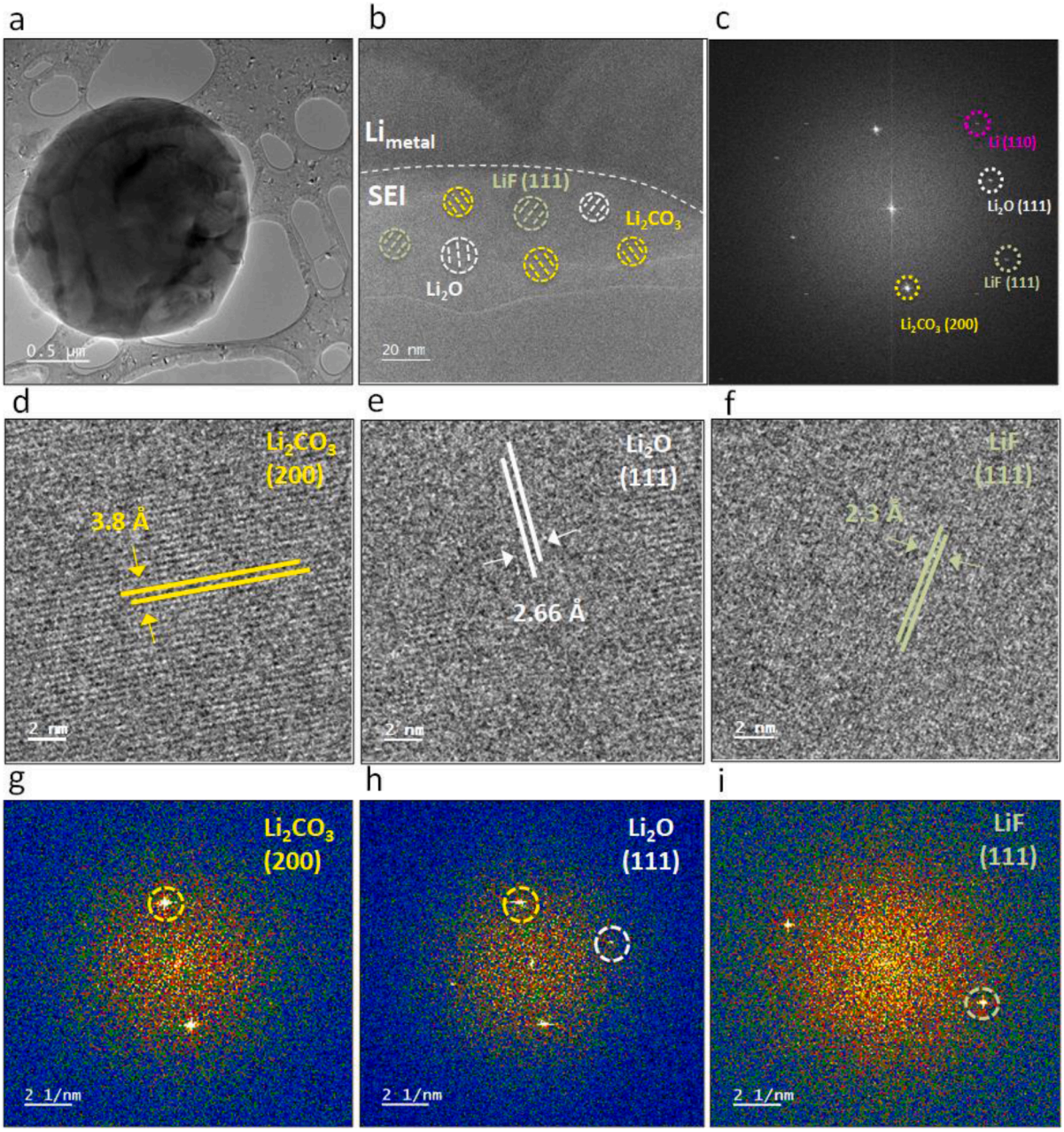


**Fig. 3.** Nanostructure of the electrochemically deposited Li metal and the corresponding SEI layer in the Li|C-SPE interface after the first Li platting. (a) Cryo-TEM image of electrochemically deposited Li particle at a low magnification. (b) HRTEM showing distribution of the components of the SEI. (c) The corresponding FFT pattern of the region shown in (b). Representative HRTEM and FFT pattern of $Li_2CO_3$ (d, g), $Li_2O$ (e, h), and LiF (f, i) in the SEI layer.

are identified to be mainly composed of $Li_2O$, LiF and $Li_2CO_3$ by matching the corresponding lattice spacings (Fig. 3d-f). Lattice spacings of 2.66 Å, 2.3 Å and 3.8 Å match well with (200), (111), and (111) planes of $Li_2CO_3$, $Li_2O$, and LiF, respectively. Moreover, the rings observed in the FFT patterns of the high-resolution images (Fig. 3g-i) further indicate the presence of $Li_2CO_3$, $Li_2O$, and LiF nanocrystals in the SEI layer. The ceramic-like crystalline grains of LiOH, $Li_2O$, and $Li_2CO_3$ are known to own low bulk Li ion conductivity, making Li ions conduction pathways to mostly present at the nanocrystals-polymer interface [53,55].

The SEI layer formed at the Li|P-SPE interface also shows a mosaic structure where traditional Li-based nanocrystals ($Li_2O$, LiOH, $Li_2CO_3$, and LiF) are embedded in an amorphous organic/polymeric phase (Fig. 4b,c). In contrast to the SEI layer in C-SPE, the Li|P-SPE interphase is rich in $Li_3N$, $Li_3P$, and $Li_3PO_4$. These nanocrystals are known to possess high Li ion conductivity, high mechanical strength and superior stability against Li metal (Table S2) [19,47,56]. The presence of crystalline nanograins is also confirmed by FFT patterns (Fig. 4c). Particularly, the indexed crystal structures of $Li_3N$, $Li_3P$, and $Li_3PO_4$ are presented in Fig. 4d-f. Using the FFT patterns (Fig. 4g-i), $Li_3N$, $Li_3P$, and $Li_3PO_4$ with d-spacings of 3.8 Å, 3.3 Å, 3.6 Å and 5.2 Å and lattice aligning along (001), (101), (010) and (011), respectively, are identified [51,54,57]. It should be noted that in contrast to the SEI layer in the C-SPE being mostly amorphous (Fig. 3b,c), the phosphazene-modified SEI layer consists of abundant crystalline nanograins (Fig. 4b,c). Thus, it can be expected that the engineered interface with high ionic conductivity leads to a significant improvement in Li ions transport at the interface, resulting in an enhanced electrochemical performance and lifespan of LMBs. Furthermore, and considering the higher stability against Li metal and higher mechanical strength of the modified SEI

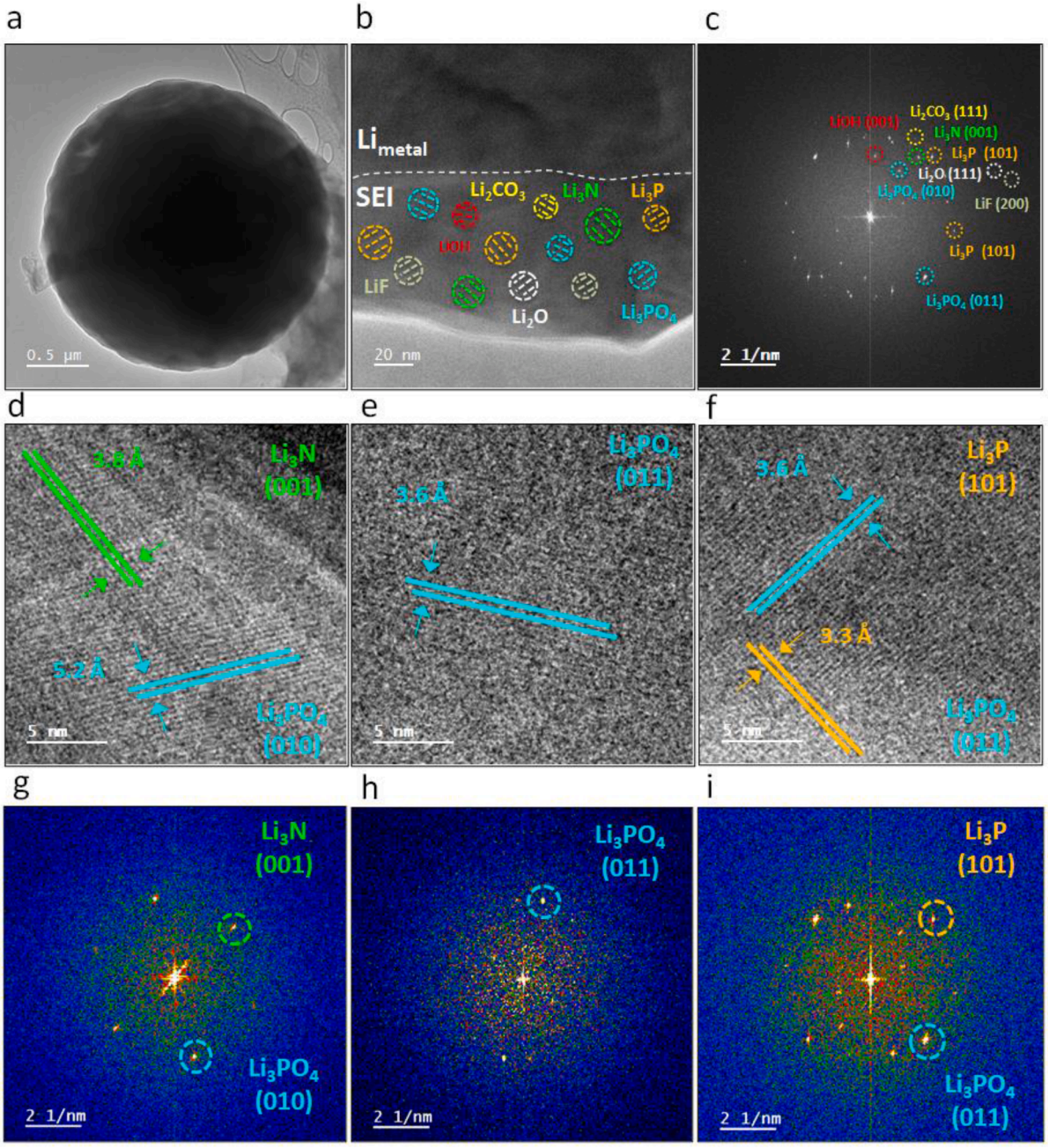


**Fig. 4.** Nanostructure of electrochemically deposited Li metal and the corresponding SEI in Li|P-SPE interface after the first Li platting. (a) Cryo-TEM image of electrochemically deposited Li particles at a low magnification. (b) HRTEM showing distribution of the components of the SEI. (c) The corresponding FFT pattern of the region shown in (b). Representative HRTEM images and FFT patterns of $Li_3N$ (d, g), $Li_3PO_4$ (e, h), and $Li_3P$ (f, i) in the SEI layer.

components (Table S2), the engineered SEI can boost the electrochemical performance and lifespan of LMBs.

### 2.4. Surface elemental analysis of the SEI layer on the Li metal anode

By employing scanning transmission electron microscopy (STEM) coupled with EDS in cryo-TEM, the elemental distribution of C, N, O, F, and P in the SEI layer is spatially mapped (Figs. S6 and S7). A significant difference in the chemical composition can be identified for the SEI film formed in the C-SPE and P-SPE. XPS analyses (Figs. 5a-e, S8) were performed to further investigate the elemental composition of the surface of the Li metal anode within Li||LFP cells with control and modified SPEs after 100 charge/discharge cycles. The XPS results for N1s, F1s, and P2p are shown in Fig. 5a-e, and the XPS results for Li1s, C1s and O1s are shown in Fig. S8. Based on the findings and consistent with the cryo-TEM results, both the Li|C-SPE interface and the Li|P-SPE interface are composed of LiOH, $Li_2O$, $Li_2CO_3$, $Li_3N$, and LiF. Deconvolution of the N1s peak for the C-SPE exhibit two peaks at ~401 eV and ~402 eV, corresponding to $NSO_x$ and $Li_3N$, respectively. The $NSO_x$ and $Li_3N$ peaks originate from decomposition of the LiTFSI salt in the C-SPE. A similar result is obtained in the case of P-SPE for the N1s peak after deconvolution. However, $Li_3N$ to $NSO_x$ ratio is significantly higher in the case of P-SPE when compared to the C-SPE. The higher ratio of $Li_3N$ nanocrystals formed at the Li metal|P-SPE interface denotes the formation of $Li_3N$ by phosphazene decomposition within the P-SPE. Deconvolution of the F1s peak for the C-SPE exhibits two peaks at ~688 eV and ~692 eV, corresponding to C-F and LiF, respectively. The LiF in SEI layer formed in PEO-based polymer electrolytes is also shown by cryo-TEM and XPS

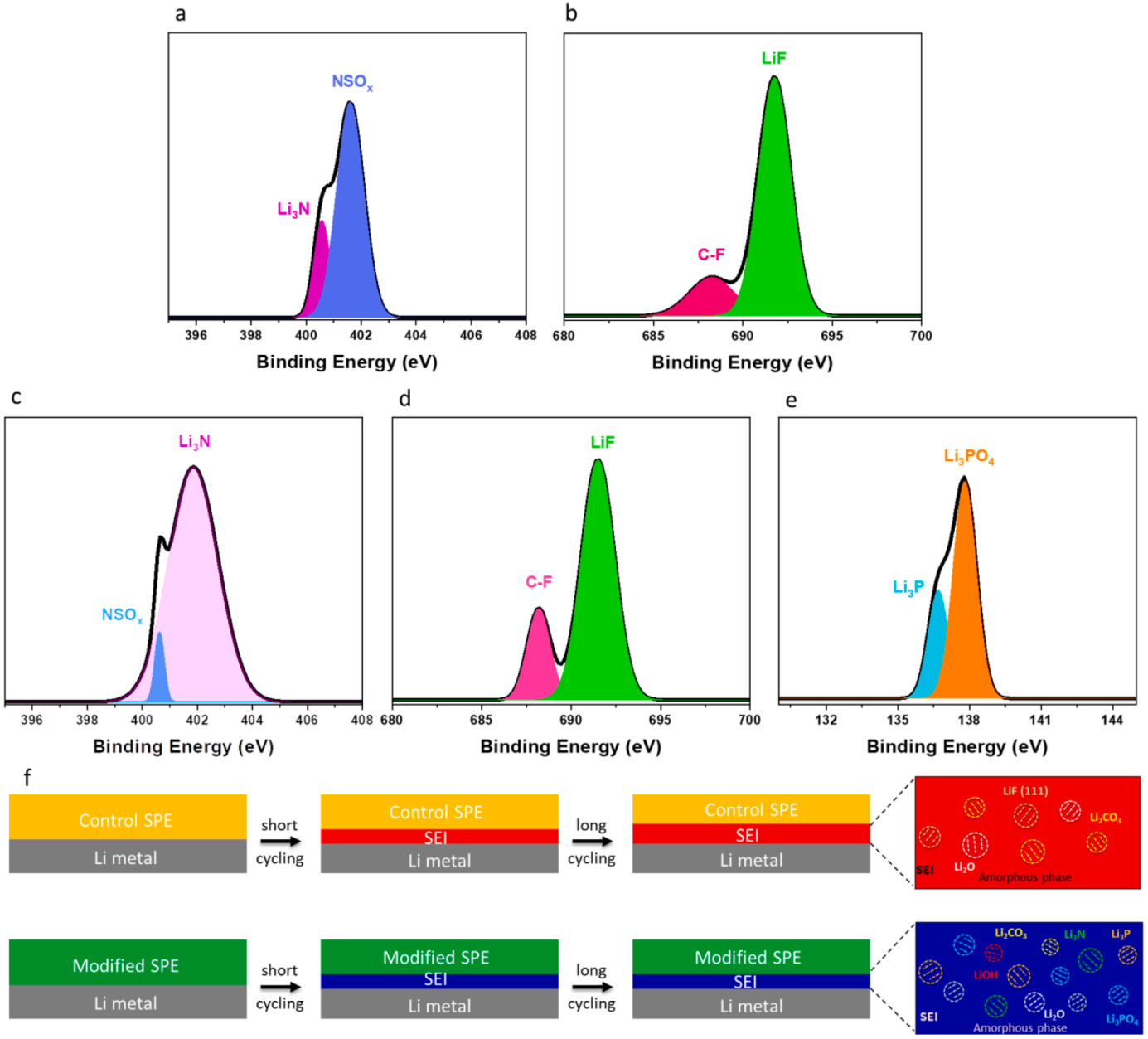


**Fig. 5.** The XPS analysis of the Li electrode surface obtained from Li||LFP cells with the C-SPE and the P-SPE after 100 charge/discharge cycles. $Li_3N$ and LiF identification in the SEI layer formed in the C-SPE (a,b) and $Li_3N$, LiF, $Li_3P$, $Li_3PO_4$ identification in the SEI layer formed in the P-SPE (c-e). Dark solid line indicates the fitting line. (f) Schematic illustration of Li platting and the SEI layer formation in the C-SPE and P-SPE.

studies elsewhere [52,53]. It is also important to note that similar to the cryo-TEM results, our XPS results also show that the SEI layer formed in the P-SPE is richer in $Li_3N$ and LiF when compared to the SEI layer formed in the C-SPE. Furthermore, the presence of phosphorous-based peak in the case of the P-SPE further indicates the electrochemical decomposition of the phosphazene additive in the P-SPE. Deconvolution of P 2p peak shows two peaks at ~137 eV and ~138 eV, corresponding to $Li_3P$ and $Li_3PO_4$, respectively. The XPS results is agreement with the cryo-TEM results at which the SEI layer formed in the P-SPE is highly crystalline and rich in $Li_3N$, LiF, $Li_3P$ and $Li_3PO_4$ nanocrystals.

A schematic illustration of the morphological features of electrochemically deposited Li and chemistry of the Li|C-SPE and Li|P-SPE interfaces is shown in Fig. 5f. Due to numerous advantages including low electronic conductivity, high electrochemical stability, high mechanical modulus, low energy barrier for Li ions surface conductivity and diffusion, LiF, $Li_3N$ and $Li_3P$ are among the most desired component in SEI [53,58]. Enhancement in electrochemical performance with LiF-rich and $Li_3N$-rich interfaces is reported in previous studies [52,53,57,59]. It is shown that low energy barrier for Li ions diffusion at LiF surface promotes Li ions migration along LiF-surface, regulating the homogeneous of Li ions flux. While bulk LiF crystals are poor Li ion conductors (Table S2), its interfaces with other crystalline grains in the SEI (e.g. $Li_2O$, $Li_2CO_3$) at the nanoscale is shown to possess high Li ion conductivity [53,55]. Furthermore, nanostructured LiF in the SEI is also reported to induce uniform diffusion field gradient in Li metal electrode [48].

### 2.5. *Theoretical simulations for the phosphazene decomposition over the Li metal surface*

The cryo-TEM (Fig. 4) and XPS (Fig. 5) results confirm the formation of LiF, $Li_3N$, $Li_3P$, $Li_3PO_4$ in the SEI layer. Indeed, phosphazene is the

source of N, F, and P elements when decomposed, which in combination with Li ions leads to the formation of LiF, $Li_3N$, $Li_3P$ and $Li_3PO_4$ compounds. For this reason, AIMD simulations were performed to better understand the mechanism of the formation of the aforementioned compounds as a result of phosphazene decomposition over the Li (110) surface. The formation of Li (110) surface was identified experimentally (Fig. 3), thus it was taken as a basis for phosphazene decomposition. Firstly, Li (110) surface was created after DFT optimization of Li bcc bulk structure, followed up by AIMD simulations of vertical (Fig. 6a) and horizontal (Fig. 6b) phosphazene orientation over Li (110) surface. These two scenarios are designed to mimic a random phosphazene position with respect to Li (110) surface. In both vertical and horizontal cases, phosphazene binds to Li surface through Li−F bonding stretching ca. 1.9 Å from the surface. The AIMD simulations indicated that the vertical orientation is slightly more favorable than the horizontal one due to four Li−F bonds (Fig. 6a). However, the decomposition of both orientations leads to the formation of LiF as shown in the far-right pictures of Fig. 6. The complete sequence of decompositions shown in Fig. 6a and 6b depicts four distinguished geometries of the initial structures (0 fs), after 50 fs (second column), after 150 fs (third column), and the final structure after 600 fs (fourth column). After 50 fs P−F bonds break and new Li (110)−F bonds are formed. In addition, for the horizontal orientation (Fig. 6b), the beginning of Li (110)−O bond formation could be observed. After 150 fs the formation of LiF for both orientations could be visible with the bond length between Li and F atoms equals to 2.0 Å, perfectly matching LiF fcc structure with Li−F bond length of 2.01 Å. At this time step, the decomposition of the horizontal orientation of phosphazene leads to the formation of $Li_2O$, which is not observed for the vertical orientation. On the other side, the vertical position of the phosphazene leads to the formation of $Li_3N$ and $Li_3P$. After 600 fs of AIMD simulations several LiF components are formed for both orientations, and restructuring of $Li_3N$, $Li_3P$ and $Li_2O$ is also observed. Hence, it could be concluded that the decomposition of the phosphazene over Li surface surely leads to the formation of $Li_2O$, LiF, $Li_3N$, and $Li_3P$ (Fig. 3). Similar behavior is also reported by Bai et al. which observe the spontaneous reaction of phosphazene with the Li metal anode [32]. Using DFT calculation, the LUMO energy of phosphazene was found to be lower than the electrochemical potential of Li metal. This indicates that the Li anode electrons could spontaneously be transferred to unoccupied orbital of the phosphazene, causing its degradation.

The formation of $Li_3PO_4$ was not observed in our AIMD simulations. We have considered several scenarios with the extended slabs and phosphazene orientations, however, the formation of $Li_3PO_4$ was not detected. Two most plausible reasons are that $Li_3PO_4$ forms under different conditions or after extended period of time, which is not possible in the accurate AIMD simulations. We have further conducted the DFT calculations to evaluate the stability of grain boundary (GB) formed between the AIMD species (Fig. S9). Specifically, the GB between Li (110) and $Li_2O$ (111), Li (110) and LiF (200), Li (110) and LiF (111), Li (100) and $Li_3N$ (0001) and Li (110) and $Li_3P$ ($10\bar{1}1$) were explored. It should be noted that all of these surface orientations were identified experimentally by Cryo-TEM (Figs. 3 and 4). Among five considered GBs, the most stable GB with the energy of 0.412 J $m^{-2}$ is the GB between Li (110) and $Li_2O$ (111), follow up by Li (110) and LiF (200) (0.485 J $m^{-2}$), Li (110) and LiF (111) (0.509 J $m^{-2}$), Li (110) and $Li_3P$ ($10\bar{1}1$) (0.632 J $m^{-2}$) and Li (110) and $Li_3N$ (0001) (0.658 J $m^{-2}$). Lower value of GB energy describes a stronger cohesive bonding between the two grains in contact. Comparing the obtained five GB energetics, we can conclude that all of them are nominally stable considering their small difference. These DFT calculation results are in agreement with the similar GB structures (although with different surface orientation) obtained by Ramasubramanian et al. [55]., who performed various DFT calculation to identify stable GBs in Li|SEI.

### 2.6. *Long-term cycle performance of LMBs with the control and modified SPEs*

The long-term cycle performance of LMBs (cathode mass loading of ~2 mg $cm^{-2}$) with the control and modified SPEs is exhibited in Fig. 7. The corresponding charge/discharge profiles of the Li||LFP cells with the control and modified SPEs are also shown in Figs. S10 and S11. The long-term cyclability results indicate that the Li||LFP cell with the C-SPE delivers an initial capacity of ~130 mAh $g^{-1}$ with less than 30% capacity retention after 500 cycles at 1C charge/discharge rate (Fig. 7a). The charge/discharge profile of the Li||LFP cell with the C-SPE (Fig. S12) indicates that the LMBs can reach to the theoretical capacity at low charge/discharge rate. In contrast, Li||LFP cell with the P-SPE (Fig. 7b)

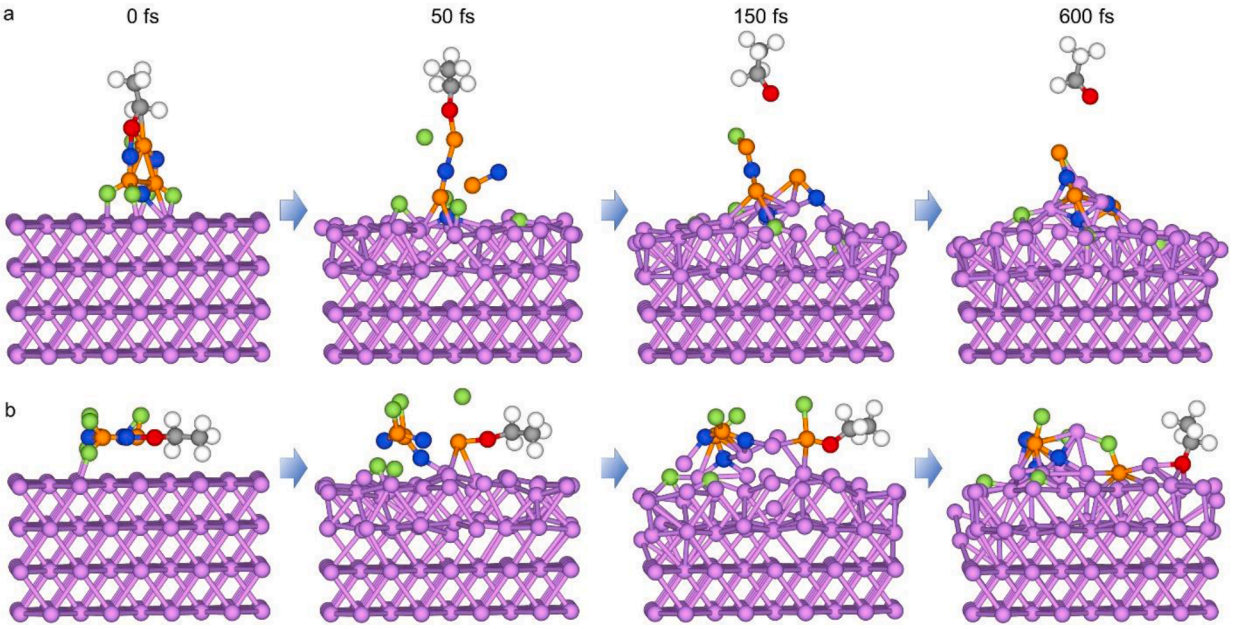


**Fig. 6.** The AIMD simulation results depicting vertical (a) and horizontal (b) phosphazene decomposition over the Li (110) surface, leading to LiF formation. Red spheres are the O atoms, lavender spheres denote Li atoms, green spheres are F atoms, blue spheres illustrate N atoms and orange spheres are P atoms.

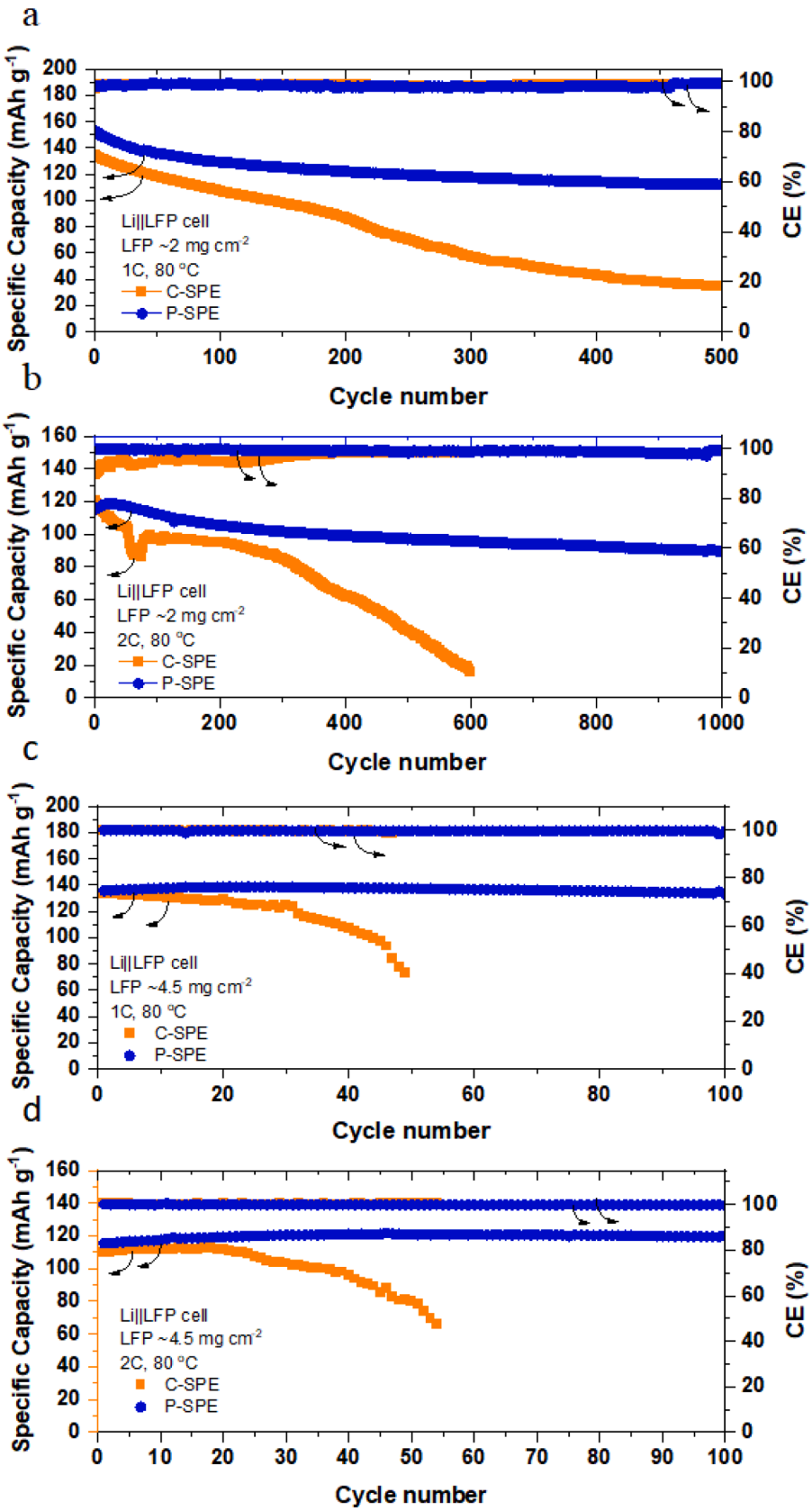


**Fig. 7.** Long-term cycle performance of LMBs with the C-SPE and the P-SPE. (a) Cycle performance of Li||LFP cells with the control and modified SPEs at 1C charge/discharge rate. The LFP cathode mass loading is ~2 mg $cm^{-2}$. (b) Cycle performance of Li||LFP cells with the control and modified SPEs at 2C charge/discharge rate. The LFP cathode mass loading is ~2 mg $cm^{-2}$. (c) Cycle performance of Li||LFP cells with the control and modified SPEs at 1C charge/discharge rate. The LFP cathode mass loading is ~4.5 mg $cm^{-2}$. (d) Cycle performance of Li||LFP cells with the control and modified SPEs at 2C charge/discharge rate. The LFP cathode mass loading is ~4.5 mg $cm^{-2}$.

shows low voltage polarization and an initial capacity of ~150 mAh $g^{-1}$ and up to 80% capacity retention after 500 cycles at 1C charge/discharge rate. Similar results are observed for the LMBs cycled at 2C charge/discharge rate. In particular, the Li||LFP cells with the C-SPE and P-SPE show an initial charge/discharge capacity of ~120 at 2C charge/discharge rate. While ~80% capacity retention is observed for the LMB with P-SPE after 1000 cycles, the LMB with the C-SPE fails (less than 5% capacity retention). The cycle performance of Li||LFP cells (the cathode mass loading of ~4.5 mg $cm^{-2}$) with the C-SPE and P-SPE is also shown in Fig. 7c,d. The corresponding charge/discharge profiles are also shown in Figs. S13 and S14. As can be seen, the Li||LFP cells with the P-SPE deliver specific capacity of ~140 mAh $g^{-1}$ and ~120 mAh $g^{-1}$ at 1C and 2C charge/discharge rates, respectively. These capacity values are higher than the Li||LFP cells with the C-SPE. In contrast to the full cell with the C-SPE which fails after around 50 cycles, the full cell with the P-SPE demonstrates an almost full capacity retention after 100 cycles at 1C and 2C charge/discharge rates, respectively. Our reported lifespan for LMBs for the developed P-SPE exceeds the lifespan for majority of the LMBs with solid-state electrolytes reported in recent years (see Table S3 and Table S4 for comparison) [60–63]. Furthermore, the Li||LFP cell with the commercial LFP (cathode mass loading of ~7.1 mg $cm^{-2}$) also delivers a specific capacity of ~180 mAh $g^{-1}$ with full capacity retention after 20 cycles at 0.2C charge/discharge rate (Fig. S15). The superior cycle performance of LMB with the phosphazene-modified SPE can be attributed to favorable chemistry and structure of SEI layer at the interphase of Li metal and SPE. The enrichment of the SEI layer with nanocrystals that own high Li ion conductivity, high mechanical strength and superior stability against Li metal promote a smooth or dense Li deposition, as well as facilitating Li ions transport which enables uniform Li platting.

## 3. Conclusion

In summary, we engineered a stable SEI layer with high Li ion conductivity at the interface of Li metal and PEO-based SPE. This is achieved by adding the phosphazene additive to the SPE which could decompose at ~3 V, leading to *in situ* nitriding, fluorinating, and phosphating of the SEI layer. In contrast to the C-SPE, a uniform and non-dendritic Li electrodeposition in the phosphazene-modified SPE is observed. Using cryo-TEM, we identified the nanoscale chemistry and structure of the SEI layer formed in the battery cells with the C-SPE and P-SPE. The SEI layer in the case of C-SPE exhibit a mostly amorphous mosaic-type SEI layer that is expected to own poor Li ion conductivity. In contrast, the mosaic-type SEI layer formed in the case of P-SPE is found to be highly crystalline and rich in $Li_3N$, LiF, $Li_3P$ and $Li_3PO_4$ nanocrystals. The decomposition of phosphazene molecules and formation of such Li compounds were also confirmed experimentally by XPS and further verified by AIMD calculations. Owning to low Li ion diffusion barrier, high stability against Li metal, high mechanical strength, and superior electronic insulation, $Li_3N$, LiF, $Li_3P$ and $Li_3PO_4$ are considered to be excellent interfacial components for Li batteries. We believe the presence of these stable crystallites with high ionic conductivity leasd to effective regulation of Li ions transport, resulting in uniform Li platting. The Li|Li cells with the P-SPE illustrate a low voltage polarization at 0.2 mA $cm^{-2}$ current density and long lifespan (1800 cycles). Furthermore, the Li||LFP cells with the P-SPE display a specific capacity of ~150 mAh $g^{-1}$ and ~120 mAh $g^{-1}$ at 1C and 2C charge/discharge rates, respectively, with up to 80% capacity retention after 500 and 1000 cycles, respectively, and >99% Coulombic efficiency.

Overall, tuning the electrolyte composition is considered one of the most effective approaches to tailor the SEI layer properties and elongating LMBs lifespan. The simple and effective approach in this study to modify the SEI layer at nanoscale offers new insights for polymer electrolytes research.

## 4. Experimental section

### 4.1. Materials

Polyethylene oxide (PEO) with molecular weight of 1000,000 g/mol, anhydrous acetonitrile, polyvinylidene fluoride (PVdF) with molecular weight of 534,000 g/mol, and N-Methyl-2-pyrrolidone (NMP) are purchased from Fisher Scientific. Lithium bis(trifluoromethanesulfonyl) imide (LiTFSI) is purchased from Sigma-Aldrich. Li metal disk, super-P carbon black (+99%), and ethoxy(pentafluoro)cyclotriphosphazene are purchased from Alfa Aesar. Lithium iron phosphate (LFP) is purchased from MTI.

### 4.2. Solid polymer electrolyte (SPE) preparation

PEO (1 g) and LiTFSI (0.45 g) are dissolved in 20 ml acetonitrile at 60 °C and the resulting mixture is stirred for at least 24 h. Then, the resulting solution is casted into a PTFE petri dish and dried at 60 °C under vacuum. To synthesize the modified SPE, a similar procedure is used except 2 wt.% ethoxy(pentafluoro)cyclotriphosphazene is dispersed into the PEO-LiTFSI SPE. The control PEO-LiTFSI SPE (C-SPE) and phosphazene-modified PEO-LiTFSI SPE (P-SPE) are stored in Ar-filled glove box. Thickness of the SPEs is approximately 100 μm.

### 4.3. Cell design

For electrolyte stability test, Li||Li symmetric cells are prepared by sandwiching the SPEs between two symmetric Li disks. Similarly, Li||LFP cells are prepared using a Li disk, a LFP electrode and the control and phosphazene-modified SPEs. To prepare LFP cathode, a homogenous slurry consisting of 70 wt.% LFP, 15 wt.% Super-P carbon black, and 15 wt.% PVdF in NMP solvent is casted onto Al current collector by a doctor blade coating machine. The resulting film is dried at 60 °C for 1 hour and then 80 °C for 24 h under vacuum and cut into circular disks using a punch machine. Two different LFP cathodes with the active material mass loadings of ~2 mg $cm^{-2}$ and ~4.5 mg $cm^{-2}$ are prepared. Furthermore, the Li||LFP cell with the commercial LFP (cathode mass loading of ~7.1 mg $cm^{-2}$, NEI) is also prepared. 2032 coin-type cells are assembled inside the glove box.

### 4.4. General characterization

Differential scanning calorimetry (DSC) is performed on TA Instruments DSC Q2000 at temperature range of −90 to 100 °C (±0.1% precision) with heating rate of 10 °C/min. Thermogravimetry analysis (TGA) is carried out using TA Instruments TGA Q5000 by heating the samples at a heating rate of 10 °C/min under $N_2$ gas atmosphere. Small SPEs with approximately 5–10 mg were cut and added to the DSC and TGA pans. Scanning electron microscopy (SEM) images are collected using a JEOL JSM-IT500HR field emission microscope operated at an accelerating voltage of 5 kV. The Li disks containing electrochemically deposited Li is prepared inside the glove box for SEM characterization by disassembling the symmetric Li|Li coin cells after five cycles of Li platting/stripping at 0.2 mA $cm^{-2}$. Dried samples are sealed in hermetic vials inside the glove box and are transferred for SEM analysis. X-Ray photoelectron spectroscopy (XPS) is performed on Thermo Scientific ESCALAB 250Xi. XPS spectra are collected using a monochromatized Al Kα radiation under a base pressure of $10^{-9}$ Torr. To avoid exposing the samples to moisture and air, samples are first loaded into an air-free XPS chamber inside the glove box and then transferred inside the XPS spectrometer. Survey scans are performed with a step size of 1.0 eV, and high-resolution scans with 0.1 eV resolution are collected for lithium (Li) 1 s, carbon (C) 1 s, oxygen (O) 1 s, nitrogen (N) 1 s, fluorine (F) 1 s, and phosphorous (P) 2p regions. Cryo-TEM images are recorded on a JEOL ARM200CF TEM, equipped with a Gatan Oneview camera operated at 200 kV. Li is electrochemically deposited onto carbon-coated Cu

grid placed on top of Cu foil within Li|C-SPE|Cu and Li|P-SPE|Cu coin cells. A constant current density of 0.2 mA $cm^{-2}$ is applied. After Li electrodeposition, the coin cells are disassembled in the glove box and TEM grid is detached from the Cu foil and rinsed with 1,3-dioxolane to remove trace electrolyte. Then, the Li metal deposited Cu grid is placed into a cryo grid box, and the grid box is placed in a vial container and sealed inside the glove box. The TEM grid then is immersed into liquid nitrogen and mounted onto a single-tilt Gatan 626 liquid nitrogen cryo-holder (Gatan, USA) using a cryo-transfer workstation. The cryotransfer station is used to ensure that the grid is under cryogenic and liquid nitrogen environment throughout the transfer process to keep the specimen in its native state.

### 4.5. Electrochemical test

Electrochemical tests are performed on BioLogic VMP3 potentiostat and Neware CT-4008 battery tester. All electrochemical experiments including electrochemical impedance spectroscopy (EIS), linear sweep voltammetry (LSV), electrolyte stability tests using Li|Li coin cells and cycle tests using Li||LFP coin cells are performed at 80 °C, unless it is stated. Electrochemical stability window of the polymer electrolytes and the phosphazene additive is evaluated by LSV and CV using a stainless disk as the working electrode and a Li disk as the counter and reference electrode. The voltammograms are recorded between open-circuit voltage up to 5 V (vs. $Li|Li^{+}$) at a sweep rate of 0.5 mV $s^{-1}$. For Li ions conductivity tests using EIS, the electrolytes are sandwiched between two stainless-steel discs with 15 mm diameter as blocking electrodes. The EIS data is collected in the frequency range of 1 MHz to 100 mHz in a temperature range from 20 °C to 100 °C, regulated by a climate chamber. The Li ion conductivity is calculated using the equation $\sigma = L/R_b \times S$, whereas σ is the Li ion conductivity (S $cm^{-1}$), $R_b$ is the bulk electrolyte resistance (Ω), L is the thickness of the electrolyte (cm), and S is the surface area of the electrolyte in contact with the stainless-steel disk. The long-term stability against Li metal for the C-SPE and P-SPE are measured on symmetric Li|Li cells under a constant current density of 0.2 mA $cm^{-2}$, with a 30 min platting/stripping for each cycle. Long-term cycle performance of Li||LFP cells made using the C-SPE and P-SPE are tested at 1C and 2C charge/discharge rates with a voltage cut-off of 4 V and 2.5 V for charging and discharging, respectively. The rate performance of the C-SPE and P-SPE at different charge/discharge rates is also explored. 1C-rate corresponds to a current density of around 160 $mAg^{-1}$.

### 4.6. Computational details

Ab-initio molecular dynamics (AIMD) and DFT simulations are performed using the Vienna Ab Initio Simulations Package (VASP) [64] code using the generalized-gradient approximation (GGA) [65] via the PBE (Perdew, Burke, and Ernzerhof) [66] functional to take into consideration the exchange-correlation effects. The system expands in x and y directions, while z direction is chosen to be perpendicular to the Li surface. The AIMD simulations were performed for 600 fs under the canonical ensemble (NVT) condition with Nosé-Hoover chain thermostat at 300 K and time step of 1 fs. For all calculations, a cutoff energy of 450 eV is used. The electronic and ionic self-consistent convergence was set to $10^{-4}$ and $10^{-3}$ eV, respectively. A Gaussian smearing with the width of 0.05 eV was employed to improve self-consistent convergence. The Li (110) surface was created using a slab method from the optimized Li bulk ground-state structure. The Gamma k-point only sampling of the Brillouin zone was used for AIMD calculations, while $2 \times 2 \times 1$ sampling was used for Li (110) optimization.

The experimentally observed different surface orientations of $Li_2O$, LiF, $Li_3N$ and $Li_3P$ grains are cleaved to form the GBs and are optimized (i.e., the minimization of total energy) until energy converting criteria are met. The GB energy is evaluated using the optimized ground state GB structure. The GB energy is calculated using the following equation:

$$\gamma_{GB} = \frac{E_{GB}^{G1/G2} - N_{G1}E_{G1} - N_{G2}E_{G2}}{2S}, \quad (1)$$

where, $\gamma_{GB}$ is the GB energy; $E_{GB}^{G1/G2}$ is the total energy of the relaxed GB structure formed by joining two cleaved interfaces; $E_{G1}$ and $E_{G2}$ are the bulk energies of two jointed structures (e.g., $Li_2O$ (111) and Li (110); $N_{G1}$ and $N_{G2}$ are number of unit cells of first and second grain, respectively, and S is the surface area of the G1 and G2 interface. For all calculations at least 15 Å vacuum space is used. Additionally, in order to ensure that the slab thickness is chosen properly and represents the properties of the macroscopic crystal structure, the GB energy is calculated for two different slab thicknesses. In general, depending upon the system, the GB energy changes by ca. 2% comparing to the increase of the slab thickness by the length of one unit cell. For all DFT and AIMD calculations, the Atomistic Tool Kit (ATK)[40] "Interface Builder" tool is used, which allows to analyze all possible interphases between two slabs. The ATK algorithm for the GB formation considers all possible repetitions and rotations (with every 2° steps) of the two given surfaces in order to find a common supercell with the lowest strain. Since there are several possibilities between two different grains of the SEI, we apply specific selection conditions, i.e., the interphase width should be ~2 Å, and the strain of each surface should be less than 5%.

## CRediT authorship contribution statement

**Vahid Jabbari:** Conceptualization, Methodology, Data curation, Writing – original draft, Writing – review & editing, Visualization, Investigation, Validation. **Vitaliy Yurkiv:** Software, Investigation, Data curation, Funding acquisition. **Md Golam Rasul:** Data curation. **Abhijit H. Phakatkar:** Data curation. **Farzad Mashayek:** Software, Supervision, Funding acquisition. **Reza Shahbazian-Yassar:** Supervision, Project administration, Writing – review & editing, Formal analysis, Funding acquisition.

## Declaration of Competing Interest

The authors declare that they have no known competing financial interests or personal relationships that could have appeared to influence the work reported in this paper.

## Acknowledgments

R. Shahbazian-Yassar acknowledges the financial support from the National Science Foundation (NSF-CBET award no. 1805938). The present DFT calculations were performed on the High-Performance Computing Cluster Extreme at the University of Illinois at Chicago. The authors also acknowledge the Battery Technology Laboratory of the College of Engineering and Research Resources Center (RRC) at the University of Illinois at Chicago (UIC) especially Director of Electron Microscopy Core, Dr. Fengyuan Shi, and Northwestern University Atomic and Nanoscale Characterization Center (NUANCE) especially NUANCE-TEM facility manager, Dr. Xiaobing Hu, and NUANCE-Keckll manager, Dr. Xinqi Chen.

## Supplementary materials

Supplementary material associated with this article can be found, in the online version, at doi:10.1016/j.ensm.2023.02.009.

## References

[1] W. Xu, J. Wang, F. Ding, X. Chen, E. Nasybulin, Y. Zhang, J.G. Zhang, Lithium metal anodes for rechargeable batteries, Energy Environ. Sci. 7 (2014) 513–537, https://doi.org/10.1039/c3ee40795k.
[2] D. Dong, B. Zhou, Y. Sun, H. Zhang, G. Zhong, Q. Dong, F. Fu, H. Qian, Z. Lin, D. Lu, Y. Shen, J. Wu, L. Chen, H. Chen, Polymer electrolyte glue: a universal

interfacial modification strategy for all-solid-state Li batteries, Nano Lett. 19 (2019) 2343–2349, https://doi.org/10.1021/acs.nanolett.8b05019.
[3] X. Chen, W. He, L.X. Ding, S. Wang, H. Wang, Enhancing interfacial contact in all solid state batteries with a cathode-supported solid electrolyte membrane framework, Energy Environ. Sci. 12 (2019) 938–944, https://doi.org/10.1039/c8ee02617c.
[4] S. Choudhury, S. Stalin, D. Vu, A. Warren, Y. Deng, P. Biswal, L.A. Archer, Solid-state polymer electrolytes for high-performance lithium metal batteries, Nat. Commun. 10 (2019) 1–8, https://doi.org/10.1038/s41467-019-12423-y.
[5] V. Jabbari, V. Yurkiv, M.G. Rasul, M. Cheng, P. Griffin, F. Mashayek, R. Shahbazian-Yassar, A smart lithium battery with shape memory function, Small 2102666 (2021) 1–11, https://doi.org/10.1002/smll.202102666.
[6] V. Jabbari, V. Yurkiv, M.G. Rasul, M.T. Saray, R. Rojaee, F. Mashayek, R. Shahbazian-Yassar, An efficient gel polymer electrolyte for dendrite-free and long cycle life lithium metal batteries, Energy Storage Mater. 46 (2022) 352–365, https://doi.org/10.1016/j.ensm.2022.01.031.
[7] Q. Zhou, J. Ma, S. Dong, X. Li, G. Cui, Intermolecular chemistry in solid polymer electrolytes for high-energy-density lithium batteries, Adv. Mater. 1902029 (2019) 1–21, https://doi.org/10.1002/adma.201902029.
[8] M. Ebadi, C. Marchiori, J. Mindemark, D. Brandell, C.M. Araujo, Assessing structure and stability of polymer/lithium-metal interfaces from first-principles calculations, J. Mater. Chem. A 7 (2019) 8394–8404, https://doi.org/10.1039/c8ta12147h.
[9] C. Wang, T. Wang, L. Wang, Z. Hu, Z. Cui, J. Li, S. Dong, X. Zhou, G. Cui, Differentiated lithium salt design for multilayered peo electrolyte enables a high-voltage solid-state lithium metal battery, Adv. Sci. 1901036 (2019) 1–10, https://doi.org/10.1002/advs.201901036.
[10] X. Zhang, S. Wang, C. Xue, C. Xin, Y. Lin, Y. Shen, L. Li, C.W. Nan, Self-suppression of lithium dendrite in all-solid-state lithium metal batteries with poly(vinylidene difluoride)-based solid electrolytes, Adv. Mater. 1806082 (2019) 1–9, https://doi.org/10.1002/adma.201806082.
[11] J. Wu, Z. Rao, Z. Cheng, L. Yuan, Z. Li, Y. Huang, Ultrathin, flexible polymer electrolyte for cost-effective fabrication of all-solid-state lithium metal batteries, Adv. Energy Mater. 1902767 (2019) 1–8, https://doi.org/10.1002/aenm.201902767.
[12] S. Li, W. Zhang, Q. Wu, L. Fan, X. Wang, X. Wang, Z. Shen, Y. He, Y. Lu, Synergistic dual-additive electrolyte enables practical lithium-metal batteries, Angew. Chem. Int. Ed. 59 (2020) 14935–14941, https://doi.org/10.1002/anie.202004853.
[13] Y. Liu, D. Lin, Y. Li, G. Chen, A. Pei, O. Nix, Y. Li, Y. Cui, Solubility-mediated sustained release enabling nitrate additive in carbonate electrolytes for stable lithium metal anode, Nat. Commun. 9 (2018) 1–10, https://doi.org/10.1038/s41467-018-06077-5.
[14] H. Zhou, S. Yu, H. Liu, P. Liu, Protective coatings for lithium metal anodes: recent progress and future perspectives, J. Power Sources 450 (2020), 227632, https://doi.org/10.1016/j.jpowsour.2019.227632.
[15] L. Lin, F. Liang, K. Zhang, H. Mao, J. Yang, Y. Qian, Lithium phosphide/lithium chloride coating on lithium for advanced lithium metal anode, J. Mater. Chem. A 6 (2018) 15859–15867, https://doi.org/10.1039/c8ta05102j.
[16] C.-.Y. Chen, T. Tsuda, Y. Oshima, S. Kuwabata, *In situ* monitoring of lithium metal anodes and their solid electrolyte interphases by transmission electron microscopy, Small Struct. 2100018 (2021) 1–7, https://doi.org/10.1002/sstr.202100018.
[17] S. Li, Q. Liu, X. Wang, Q. Wu, L. Fan, W. Zhang, Z. Shen, L. Wang, M. Ling, Y. Lu, Constructing a phosphating-nitriding interface for practically used lithium metal anode, ACS Mater. Lett. 2 (2020) 1–8, https://doi.org/10.1021/acsmaterialslett.9b00416.
[18] X.R. Chen, Y.X. Yao, C. Yan, R. Zhang, X.B. Cheng, Q. Zhang, A diffusion–reaction competition mechanism to tailor lithium deposition for lithium-metal batteries, Angew. Chem. Int. Ed. 59 (2020) 7743–7747, https://doi.org/10.1002/anie.202000375.
[19] M. Wu, Z. Wen, Y. Liu, X. Wang, L. Huang, Electrochemical behaviors of a Li3N modified Li metal electrode in secondary lithium batteries, J. Power Sources 196 (2011) 8091–8097, https://doi.org/10.1016/j.jpowsour.2011.05.035.
[20] Z. Wang, Y. Wang, C. Wu, W.K. Pang, J. Mao, Z. Guo, Constructing nitrided interfaces for stabilizing Li metal electrodes in liquid electrolytes, Chem. Sci. 12 (2021) 8945–8966, https://doi.org/10.1039/d1sc01806j.
[21] N. Tapia-Ruiz, A.G. Gordon, C.M. Jewell, H.K. Edwards, C.W. Dunnill, J. M. Blackman, C.P. Snape, P.D. Brown, I. MacLaren, M. Baldoni, E. Besley, J. J. Titman, D.H. Gregory, Low dimensional nanostructures of fast ion conducting lithium nitride, Nat. Commun. 11 (2020) 1–8, https://doi.org/10.1038/s41467-020-17951-6.
[22] S. Zhang, G. Yang, Z. Liu, X. Li, X. Wang, R. Chen, F. Wu, Z. Wang, L. Chen, Competitive solvation enhanced stability of lithium metal anode in dual-salt electrolyte, Nano Lett. 21 (2021) 3310–3317, https://doi.org/10.1021/acs.nanolett.1c00848.
[23] A.M. Tripathi, W.N. Su, B.J. Hwang, *In situ* analytical techniques for battery interface analysis, Chem. Soc. Rev. 47 (2018) 736–751, https://doi.org/10.1039/c7cs00180k.
[24] A.V. Cresce, S.M. Russell, D.R. Baker, K.J. Gaskell, K. Xu, *In situ* and quantitative characterization of solid electrolyte interphases, Nano Lett. 14 (2014) 1405–1412, https://doi.org/10.1021/nl404471v.
[25] L. Suo, Y.S. Hu, H. Li, M. Armand, L. Chen, A new class of Solvent-in-Salt electrolyte for high-energy rechargeable metallic lithium batteries, Nat. Commun. 4 (2013) 1–9, https://doi.org/10.1038/ncomms2513.
[26] W. Zhang, Z. Shen, S. Li, L. Fan, X. Wang, F. Chen, X. Zang, T. Wu, F. Ma, Y. Lu, Engineering wavy-nanostructured anode interphases with fast ion transfer kinetics: toward practical Li-metal full batteries, Adv. Funct. Mater. 30 (2020) 1–8, https://doi.org/10.1002/adfm.202003800.
[27] S. Schmohl, X. He, H.D. Wiemhöfer, Boron trifluoride anionic side groups in polyphosphazene based polymer electrolyte with enhanced interfacial stability in lithium batteries, Polymers 10 (2018) 1350, https://doi.org/10.3390/polym10121350 (Basel).
[28] S. Jankowsky, M.M. Hiller, H.D. Wiemhöfer, Preparation and electrochemical performance of polyphosphazene based salt-in-polymer electrolyte membranes for lithium ion batteries, J. Power Sources 253 (2014) 256–262, https://doi.org/10.1016/j.jpowsour.2013.11.120.
[29] S. Jankowsky, M.M. Hiller, R. Stolina, H.D. Wiemhöfer, Performance of polyphosphazene based gel polymer electrolytes in combination with lithium metal anodes, J. Power Sources 273 (2015) 574–579, https://doi.org/10.1016/j.jpowsour.2014.09.077.
[30] S.H. Kang, J.K. Jang, H.Y. Jeong, S. So, S.K. Hong, Y.T. Hong, S.J. Yoon, D.M. Yu, Polyacrylonitrile/Phosphazene composite-based heat-resistant and flame-retardant separators for safe lithium-ion batteries, ACS Appl. Energy Mater. 5 (2022) 2452–2461, https://doi.org/10.1021/acsaem.1c03948.
[31] J.A. Choi, Y. Kang, D.W. Kim, Lithium polymer cell assembled by *in situ* chemical cross-linking of ionic liquid electrolyte with phosphazene-based cross-linking agent, Electrochim. Acta 89 (2013) 359–364, https://doi.org/10.1016/j.electacta.2012.11.083.
[32] W.L. Bai, Z. Zhang, X. Chen, Q. Zhang, Z.X. Xu, G.Y. Zhai, X. Lin, X. Liu, T. Tadesse Tsega, C. Zhao, K.X. Wang, J.S. Chen, Phosphazene-derived stable and robust artificial SEI for protecting lithium anodes of Li-O2batteries, Chem. Commun. 56 (2020) 12566–12569, https://doi.org/10.1039/d0cc05303a.
[33] H.R. Allcock, D.T. Welna, A.E. Maher, Single ion conductors-polyphosphazenes with sulfonimide functional groups, Solid State Ionics 177 (2006) 741–747, https://doi.org/10.1016/j.ssi.2006.01.039.
[34] K. Sahni, M. Ashuri, Q. He, R. Sahore, I.D. Bloom, Y. Liu, J.A. Kaduk, L.L. Shaw, H3PO4 treatment to enhance the electrochemical properties of Li(Ni1/3Mn1/3Co1/3)O2 and Li(Ni0.5Mn0.3Co0.2)O2 cathodes, Electrochim. Acta 301 (2019) 8–22, https://doi.org/10.1016/j.electacta.2019.01.153.
[35] N. Wu, Y. Li, A. Dolocan, W. Li, H. Xu, B. Xu, N.S. Grundish, Z. Cui, H. Jin, J. B. Goodenough, *In situ* formation of Li3P layer enables fast $Li^+$ conduction across Li/solid polymer electrolyte interface, Adv. Funct. Mater. 30 (2020) 1–6, https://doi.org/10.1002/adfm.202000831.
[36] Y.A. Du, N.A.W. Holzwarth, Mechanisms of $Li^+$ diffusion in crystalline γ- and β-$Li_3PO_4$ electrolytes from first principles, Phys. Rev. B Condens. Matter Mater. Phys. 76 (2007) 1–14, https://doi.org/10.1103/PhysRevB.76.174302.
[37] N. Hasan, M. Pulst, M.H. Samiullah, J. Kressler, Comparison of Li+-ion conductivity in linear and crosslinked poly(ethylene oxide), J. Polym. Sci. Part B Polym. Phys. 57 (2019) 21–28, https://doi.org/10.1002/polb.24750.
[38] W. Zhou, Z. Wang, Y. Pu, Y. Li, S. Xin, X. Li, J. Chen, J.B. Goodenough, Double-layer polymer electrolyte for high-voltage all-solid-state rechargeable batteries, Adv. Mater. 31 (2019) 1–7, https://doi.org/10.1002/adma.201805574.
[39] M. Zhou, C. Qin, Z. Liu, L. Feng, X. Su, Y. Chen, L. Xia, Y. Xia, Z. Liu, Enhanced high voltage cyclability of LiCoO 2 cathode by adopting poly [bis-(ethoxyethoxyethoxy) phosphazene] with flame-retardant property as an electrolyte additive for lithium-ion batteries, Appl. Surf. Sci. 403 (2017) 260–266, https://doi.org/10.1016/j.apsusc.2017.01.189.
[40] L. Xia, Y. Xia, Z. Liu, A novel fluorocyclophosphazene as bifunctional additive for safer lithium-ion batteries, J. Power Sources 278 (2015) 190–196, https://doi.org/10.1016/j.jpowsour.2014.11.140.
[41] Y. Ji, P. Zhang, M. Lin, W. Zhao, Z. Zhang, Y. Zhao, Y. Yang, Toward a stable electrochemical interphase with enhanced safety on high-voltage LiCoO2 cathode: a case of phosphazene additives, J. Power Sources 359 (2017) 391–399, https://doi.org/10.1016/j.jpowsour.2017.05.091.
[42] A. Yusuf, V. Sai Avvaru, J. De la Vega, M. Zhang, J. Garcia Molleja, D.Y. Wang, Unveiling the structure, chemistry, and formation mechanism of an *in-situ* phosphazene flame retardant-derived interphase layer in $LiFePO_4$ cathode, Chem. Eng. J. 455 (2023), 140678, https://doi.org/10.1016/j.cej.2022.140678.
[43] G.Q. Liu, Q. Hou, X.X. Fan, Q.Y. Zheng, J.K. Chang, J.M. Fan, R.M. Yuan, M. Sen Zheng, Q.F. Dong, *In situ* constructing a catalytic shell for sulfur cathode via electrochemical oxidative polymerization, ACS Appl. Mater. Interfaces (2022), https://doi.org/10.1021/acsami.2c18695.
[44] T. Dagger, B.R. Rad, F.M. Schappacher, M. Winter, Comparative performance evaluation of flame retardant additives for lithium ion batteries – I. safety, chemical and electrochemical stabilities, Energy Technol. 6 (2018) 2011–2022, https://doi.org/10.1002/ente.201800132.
[45] O. Sheng, J. Zheng, Z. Ju, C. Jin, Y. Wang, M. Chen, J. Nai, T. Liu, W. Zhang, Y. Liu, X. Tao, *In situ* construction of a LiF-enriched interface for stable all-solid-state batteries and its origin revealed by Cryo-TEM, Adv. Mater. 32 (2020) 1–10, https://doi.org/10.1002/adma.202000223.
[46] J. Zheng, Z. Ju, B. Zhang, J. Nai, T. Liu, Y. Liu, Q. Xie, W. Zhang, Y. Wang, X. Tao, Lithium ion diffusion mechanism on the inorganic components of the solid-electrolyte interphase, J. Mater. Chem. A 9 (2021) 10251–10259, https://doi.org/10.1039/d0ta11444h.
[47] Y. Li, W. Huang, Y. Li, A. Pei, D.T. Boyle, Y. Cui, Correlating structure and function of battery interphases at atomic resolution using cryoelectron microscopy, Joule 2 (2018) 2167–2177, https://doi.org/10.1016/j.joule.2018.08.004.
[48] A. Ramasubramanian, V. Yurkiv, T. Foroozan, M. Ragone, R. Shahbazian-Yassar, F. Mashayek, Lithium diffusion mechanism through solid-electrolyte interphase in rechargeable lithium batteries, J. Phys. Chem. C 123 (2019) 10237–10245, https://doi.org/10.1021/acs.jpcc.9b00436.

[49] D. Cheng, T.A. Wynn, X. Wang, S. Wang, M. Zhang, R. Shimizu, S. Bai, H. Nguyen, C. Fang, M. cheol Kim, W. Li, B. Lu, S.J. Kim, Y.S. Meng, Unveiling the stable nature of the solid electrolyte interphase between lithium metal and LiPON via cryogenic electron microscopy, Joule 4 (2020) 2484–2500, https://doi.org/10.1016/j.joule.2020.08.013.

[50] L. Wang, A. Menakath, F. Han, Y. Wang, P.Y. Zavalij, K.J. Gaskell, O. Borodin, D. Iuga, S.P. Brown, C. Wang, K. Xu, B.W. Eichhorn, Identifying the components of the solid–electrolyte interphase in Li-ion batteries, Nat. Chem. 11 (2019) 789–796, https://doi.org/10.1038/s41557-019-0304-z.

[51] O. Sheng, J. Zheng, Z. Ju, C. Jin, Y. Wang, M. Chen, J. Nai, T. Liu, W. Zhang, Y. Liu, X. Tao, *In situ* construction of a LiF-enriched interface for stable all-solid-state batteries and its origin revealed by Cryo-TEM, Adv. Mater. 32 (2020), 2000223, https://doi.org/10.1002/adma.202000223.

[52] X. Cao, X. Ren, L. Zou, M.H. Engelhard, W. Huang, H. Wang, B.E. Matthews, H. Lee, C. Niu, B.W. Arey, Y. Cui, C. Wang, J. Xiao, J. Liu, W. Xu, J.G. Zhang, Monolithic solid–electrolyte interphases formed in fluorinated orthoformate-based electrolytes minimize Li depletion and pulverization, Nat. Energy 4 (2019) 796–805, https://doi.org/10.1038/s41560-019-0464-5.

[53] W. Li, Y. Pang, J. Liu, G. Liu, Y. Wang, Y. Xia, A PEO-based gel polymer electrolyte for lithium ion batteries, RSC Adv. 7 (2017) 23494–23501, https://doi.org/10.1039/c7ra02603j.

[54] Y. Kang, K. Cheong, K.A. Noh, C. Lee, D.Y. Seung, A study of cross-linked PEO gel polymer electrolytes using bisphenol A ethoxylate diacrylate: ionic conductivity and mechanical properties, J. Power Sources 119–121 (2003) 432–437, https://doi.org/10.1016/S0378-7753(03)00183-6.

[55] M.W. Logan, S. Langevin, B. Tan, A.W. Freeman, C. Hoffman, D.B. Trigg, K. Gerasopoulos, UV-cured eutectic gel polymer electrolytes for safe and robust Li-ion batteries, J. Mater. Chem. A 8 (2020) 8485–8495, https://doi.org/10.1039/d0ta01901a.

[56] W. Fan, N.W. Li, X. Zhang, S. Zhao, R. Cao, Y. Yin, Y. Xing, J. Wang, Y.G. Guo, C. Li, A dual-salt gel polymer electrolyte with 3D cross-linked polymer network for dendrite-free lithium metal batteries, Adv. Sci. 5 (2018), 1800559, https://doi.org/10.1002/advs.201800559.

[57] G. Kresse, J. Furthmüller, Efficient iterative schemes for ab initio total-energy calculations using a plane-wave basis set, Phys. Rev. B Condens. Matter Mater. Phys. 54 (1996) 11169–11186, https://doi.org/10.1103/PhysRevB.54.11169.

[58] J.P. Perdew, J.A. Chevary, S.H. Vosko, K.A. Jackson, M.R. Pederson, D.J. Singh, C. Fiolhais, Erratum: atoms, molecules, solids, and surfaces: applications of the generalized gradient approximation for exchange and correlation, Phys. Rev. B. 48 (1993) 4978, https://doi.org/10.1103/PhysRevB.48.4978.2.

[59] J.P. Perdew, K. Burke, M. Ernzerhof, Generalized gradient approximation made simple, Phys. Rev. Lett. 77 (1996) 3865–3868, https://doi.org/10.1103/PhysRevLett.77.3865.